Enabling photodetection electronics for fluorescent diamond based quantum sensing

Vladislav Serafimov

November 26, 2025

Contents

Chapter 1

Foreword

Chapter 2

Summary

Chapter 3

Introduction

This chapter introduces the assignment and some foundational concepts of quantum sensing.

3.1   Background

Nitrogen Vacancy (NV) centers [1] are imperfections in the atomic structure of diamonds. The two types of NV centers are NV0 and NV-, as seen in Figure 3.1, but the NV- structure is much more commonly used in quantum applications. These imperfections have the useful property of spin-dependent luminescence. This means that the spin of the NV center affects the frequency of the light emitted by the structure[1]. Using this quality of the NV structure, different environmental metrics (e.g magnetic fields) can be measured.

The Applied Nanotechnology research group is working on a NV-center-based sensor setup. There exist several quantum protocols, but the one this setup needs to support is called Constant-Wave ODMR (ODMR). At its core, Optically Detected Magnetic Resonance (ODMR) is a set of protocols, which can detect magnetic fields based on the fluctuations in the fluorescence of NV centers [3]. CW-ODMR in particular involves exposing the NV center to a Microwave (MW) sweep while illuminating it with a constant light source. This is in contrast with Pulsed ODMR (ODMR) techniques, which use different Transistor-Transistor Logic (TTL) pulse schemes [4] to modulate the MW signal and the light source.

Acquiring and processing data from the setup requires working with weak signals that are hard to distinguish from the environmental noise. While this is a significant problem, it is also very common. Because of this, the industry has already adopted systems to detect weak light sources and measure their intensity. This project is mainly about developing a similar photodetection system for the NV setup.

Figure 3.1: NV0 (a) and NV- (b) structures in diamonds (image credit to Haque et al [5])

3.2   Purpose of the assignment

Implementing a Transimpedance Amplifier (TIA) is the main purpose of the assignment. To create a complete solution, there are also several additional functionalities and systems that need to be developed.

Firstly, a custom photodetector needs to be designed. The circuit should accommodate the sensors and output to a lock-in amplifier. After establishing connection, an Open Lock-In Amplifier

---

[1]The NV center only emits light after absorbing photons, a phenomenon called photoluminescence [2]

(OLIA) [2] circuit needs to be tested and compared to conventional lock-in systems. Lastly, a control interface can be implemented, if there is enough time. It needs to be programmed so that it can control all necessary features of the lock-in amplifier.

3.3 Assignment specifications

As already explained, the assignment is quite broad and involves both hardware and software, causing the need for a number of different tools.

Most of the hardware tools are already available at the Applied Nanotechnology lab. The lock-in amplifiers which will be used for the tests are the most important pieces of hardware. Zurich Instruments HF2LI is the benchmark lock-in amplifier. The target amplification is at least 10dB. Chapter 3.1 already discussed the basics of the CW-ODMR protocol. In order to get an operational CW-ODMR setup, an MW generator and a laser will be used. MW sweeping needs to be done in the range of 2,8 to 2,9 GHz and the lab already has a custom-built MW generator that can output these frequencies. The laser is mostly outside the scope of the assignment, as it is almost entirely optical in nature and the driving circuitry has been developed by a previous intern. Setting it up, together with the NV samples, is up to the client. However, it is important to note that the fluorescence wavelength is in the range of 637 to 800 nm, as it plays an important part in photodetection.

In terms of software, there is more freedom of choice. Interfacing with the HF2LI is done through proprietary software, but this is the only required program. There are various Electronic Computer-Aided Design (ECAD) software suites that offer the same base functionality. KiCad was selected because the client prefers open-source software. The program for retrieving data from the lock-in amplifiers can be written in both Python and MATLAB. Both languages have good integration with the main lock-in amplifier. They also offer Graphical User Interface (GUI) programming capabilities and are good for scientific computing overall.

3.4 Scope of work

The scope of the project was extensively discussed with the company coach. Chapter 3.4.1 sets the scope and Chapter 3.4.2 builds on it, providing more specific details.

3.4.1 Project boundaries

The project boundaries were initially based on the assignment form, but were later discussed with the client and refined further.

Must have

- Hardware platform for photodetection

- Software for signal processing and visualization

Should have

- Tests with different diamond samples

Could have

- Tests with different quantum protocols

- OLIA implementation

- Tests comparing OLIA to market solutions

Will not have

- Laser as a part of the hardware platform

- Laser driver upgrade

---

[2]OLIA is an open-source microcontroller-based lock-in amplifier. It uses common components, which makes it easy to build [6]

3.4.2   Goals

Based on the MoSCoW priorities from Chapter 3.4.1, a set of goals was created to further specify all items from each prioritization category. Every goal was designed so that its outcome results in a tangible project milestone (e.g. a deliverable).

Goal 1 : Create a hardware setup, which measures and amplifies photodiode signals

Goal 2 : Develop software to process and visualize lock-in amplifier signals

Goal 3 : Compare the performance of different lock-in amplifiers

    While these goals are practical, they are still not specific enough. To eliminate the possibility of confusion, a set of tasks were created. All tasks contribute to one of the three goals.

Task 1.1 : Design a photodiode Printed Circuit Board (PCB), which can accommodate different lock-in amplifiers

Task 1.2 : Build an operable OLIA

Task 2.1 : Develop software that acquires signals and is then able to visualize them

Task 3.1 : Use key performance metrics to compare the OLIA implementation to market solutions

Task 3.2 : Measure OLIA performance using different diamond samples and quantum protocols

    Task 1.1 involves the design and production of a photodiode PCB. The PCB has to output signals that are not only compatible with lock-in amplifiers that are available on the market, but also with the OLIA. This part of the hardware design has the highest priority, which is why it will be done first.

    Task 1.2 is to build an OLIA amplifier, which can be used at Applied Nanotechnology's laboratory. This will be done with the technical specifications and firmware provided by Harvie and de Mello [6]. The necessity for an OLIA is low, because the Applied Nanotechnology research group already has two lock-in amplifiers.

    Task 2.1 is to write an application in Python or MATLAB. This can be done on a different setup, but ideally it will use the hardware setup from **Goal 1**. Because the OLIA project uses open-source firmware that differs from proprietary solutions, there might need to be two separate applications. This task can only be completed once a measurement setup is built, so its execution will follow the first two tasks.

    Task 3.1 requires all previous tasks to be finished. The completed setup needs to be used to measure the performance of lock-in amplifiers available on the market and the OLIA implementation. Signal-to-Noise Ratio (SNR), bandwidth and stability are the main metrics that need to be compared.

    Task 3.2 is similar to **Task 3.1**, but it is a much broader exploration of the performance of the lock-in amplifiers. Using different diamond samples and quantum protocols will show how the amplifier performs and how different conditions affect it. Because the task can be used to verify the setup from **Goal 1**, it can also be done before **Task 3.1**. Tests with varying diamond samples are more important to the client, which is why they will take precedence over tests with different quantum protocols.

3.4.3   Deliverables

The description of the tasks already provided context for the deliverables, but this subsection contains a formalized version of the deliverables.

1. Photodetection PCB

2. OLIA implementation

3. Software application

4. Comparison visualization

5. Technical documentation

    The only deliverable, which was not mentioned in Chapter 3.4.2 is the technical documentation. This is because it should contain information about every task.

3.5   Methodology

The V-Model methodology was selected, as it is well-suited for low-level projects. Figure 3.2 shows a diagram of the phases of the V-Model. Unlike some software-oriented models, the V-Model is very sequential. This can sometimes be seen as detrimental, but in this case it helps with structuring the project. Another benefit of this model is that there are multiple testing activities, which underpin the quality assurance. A contentious feature of the V-Model is the heavy reliance on the initial requirements. This need for deliberate project requirements can be hard to meet, especially if the client representative is not technically proficient. However, this is not the case in this project. The requirements were extensively discussed with the client representative, based on which the project boundaries in Chapter 3.4.1 were set up.
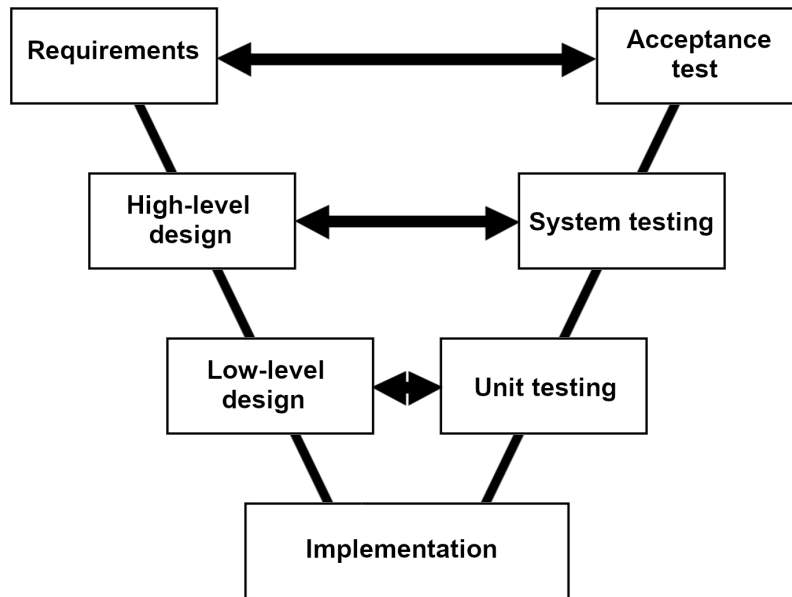

Figure 3.2: V-Model diagram

3.6   Report outline

The introduction is followed by the functional design chapter, which introduces background knowledge, needed to understand the NV setup. After that, the high-level design of the system is presented. It explains the functionality of the various systems that make up the project without delving into specifics.

After that, the technical design explores the low-level design of the systems of the project. It mentions all the necessary details, including calculations, simulations and implementation steps.

Following the design sections, the testing chapter describes the testing goals and what methods were used for measuring. The chapter then presents the test results.

Lastly, the conclusion and recommendation chapters summarize the outcomes of the project and offer proposals for further development.

Chapter 4

Functional design

4.1 Background knowledge

4.1.1 Spin states

Spin, at least in quantum mechanics, is the intrinsic angular momentum of a particle, which is described by the quantum number of the particle. Importantly, it differs from the angular momentum in classical mechanics, which is extrinsic. Spin characterizes systems of particles, usually electrons, using quantum entanglement. This phenomenon refers to the "entanglement", or spin correlation, of a set of particles.

These foundational concepts make it possible to describe quantum systems using various states. The most simple states, used as descriptors, are the energy states. Ground states refer to the system being in an energy minimum. On the other hand, excited states signify that the system has more energy than at its ground state. Additionally, there can be intermediate states during state transition.

While the aforementioned states describe system energy, they have no bearing on the spin. For the purposes of this project, only two spin states need to be explained. The first one is called singlet state. It occurs when an entangled system has a total spin of 0, caused by the mutual cancellation of spin. For example, for a system of two entangled electrons to be a singlet, the two spins would need to point in opposite directions. The second spin state is called triplet and it has a total spin of 1. Triplets can consist of, for instance, two unpaired electrons with aligned spins that sum up to 1. Singlets and triplets both have major distinguishing features and properties, which is why they can be used for quantum sensing. Aside from the difference in spin, triplets tend to have higher energy levels. They also exhibit attraction to magnetic fields, while singlets cannot be influenced directly by magnetism.

4.1.2 Zeeman effect

Discovered by Pieter Zeeman in 1896, the Zeeman effect is another important phenomenon that enables quantum sensing. If under normal circumstances a light-emitting quantum system only emits one spectral line, then when a magnetic field is applied to it the line will split, thus exhibiting the Zeeman effect. In an NV center, this phenomenon causes the $|\pm1\rangle$ energy level to split into $|+1\rangle$ and $|-1\rangle$.

4.1.3 Energy levels

Figure 4.1 shows the energy level diagram of an NV center.

After illuminating the NV center with a green laser, electrons go from a ground state to an excited state. They then need to return to the ground state. This decay process is usually direct and emits a red photon, however it can also go through the metastable singlet state and emit an infrared photon. It should be noted that whenever the NV center is exposed to the resonant frequency $\nu = 2,87 GHz$ the probability of emitting an infrared photon is significantly increased.
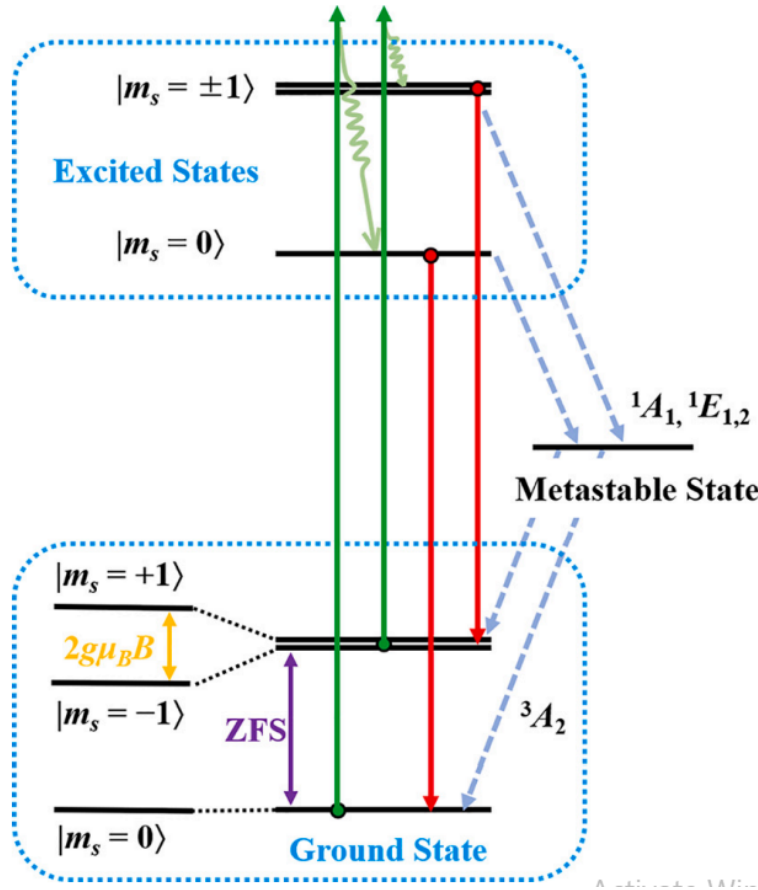
Figure 4.1: NV center energy level diagram (image credit to Song et al [7])

4.2 Quantum protocols

There are a number of different quantum protocols, which differ in what they can measure, in how precisely they can measure it and in the complexity of the hardware they require to operate. CW-ODMR is the main protocol this project is aimed at facilitating. As Saijo et al [8] demonstrate, CW-ODMR is relatively simple, while still detecting magnetic field with reasonable sensitivity. P-ODMR does outperform CW-ODMR [9], but because of the added complexity working with it is a "Could have" (see Chapter ??). Before being able to run P-ODMR on the setup at the lab, several protocols need to be implemented first [4]. T_1 measurements, which are one of the fundamentals of Magnetic Resonance Imaging (MRI), should be conducted first. Afterwards, Rabi oscillations need to be observed and measured in order to calibrate the setup. Without these intermediate protocols, P-ODMR cannot be performed.

4.2.1 CW-ODMR

CW-ODMR is a quantum protocol that has seen extensive usage in sensing setups that measure magnetic fields. Its working principle is centered around the photoluminescence of NV centers and the difference in light emission based on spin states. As already discussed in Chapter 4.1.3, the NV center emits less visible light when at the resonant frequency ν. Additionally, two more dips appear on the spectrum if a magnetic field is applied.Calculating the magnetic field can be done using the formula $h\nu = g_e\mu_B B_{AC}$[1]. Figure 4.2 shows an example of what a CW-ODMR spectrum might look like.

4.2.2 T_1 relaxometry

T_1, T_2 and T_2^* relaxation time measurements are commonly associated with radiometry [10], but they have other uses too. T_1 measurements, in particular, are useful in the realm of quantum

---

[1]3, In the formula, h is the Planck constant, g_e is the g-factor of the electron and μ_B is the Bohr magneton. Knowing all other variables, B_{AC} can easily be calculated.
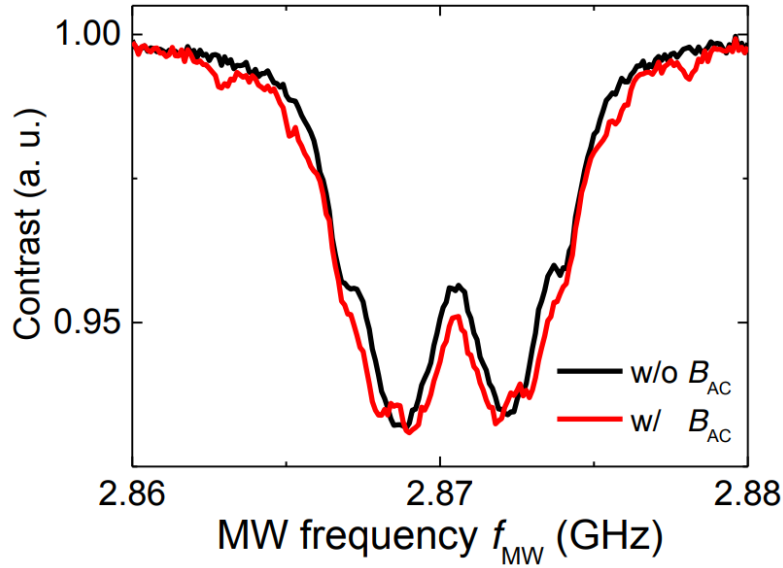
Figure 4.2: Example of a CW-ODMR spectrum **with** and **without** a magnetic field (image credit Saijo et al [8])

sensing. Knowing the T_1 relaxation time, which refers to the time it takes for the spins in an NV system to decay back to their original state, makes it possible to adjust the pulse sequences of more complex protocols and thus get better results.
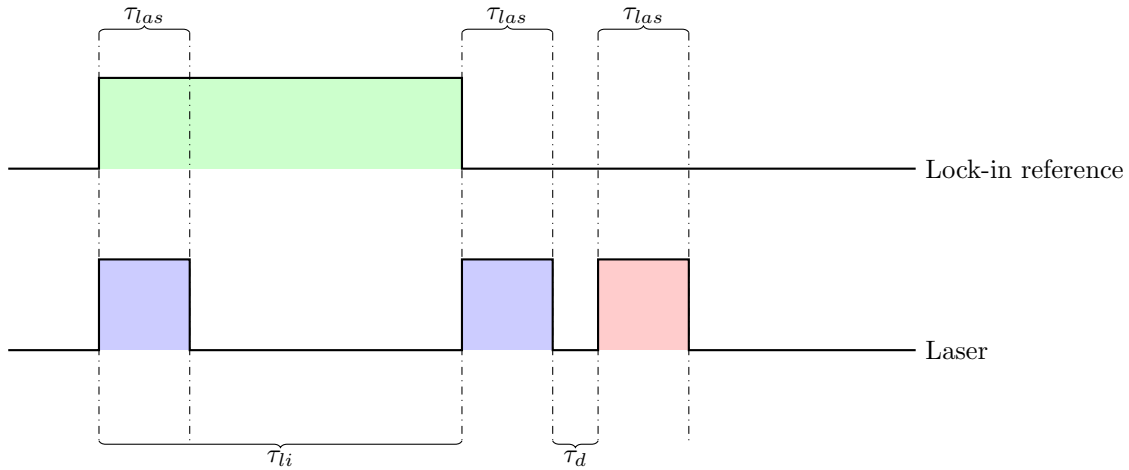

Figure 4.3: Laser and reference signals for T_1 measurements

The waveforms which are needed for T_1 measurements are shown if Figure 4.3. While both are important in practice, the lock-in is not as relevant, at least in this section of the report. However, its working principle is explored in Chapter 4.4. For now, all that needs to be said about the lock-in reference signal is that it is periodic and τ_{li} is much longer than τ_{las} (Sewani et al [4] propose $\tau_{li} = 15ms$ and $\tau_{las} = 5\mu s$). Laser pulses, on the other hand, are not periodic. Instead, there are three short pulses every reference period (which is $2\tau_{li}s$ long). The two blue pulses have the same timing every cycle, because they initialize the NV spins. However, the red pulse always occurs after the variable dark time τ_d. Depending on the T_1 decay at the time of the readout pulse, a different voltage will be detected. Figure 4.4 shows what results can be expected when measuring T_1. Determining the value of T_1 is done using Formula 4.1, where I is the light intensity, I_∞ is the light intensity offset and τ_d is the dark time.

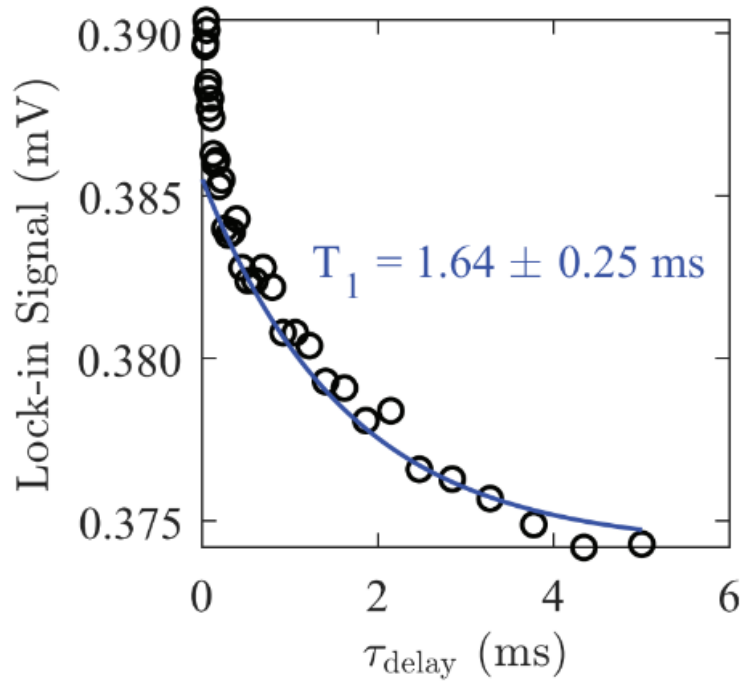$$I(t) = I_\infty + I(0)e^{-\tau_d/T_1} \tag{4.1}$$

Figure 4.4: Results of a set of T_1 measurements with varied dark time τ_d (image credit to Sewani et al [4])

4.2.3   P-ODMR

As a descriptor P-ODMR is somewhat vague, which is why it has been used for a number of protocols. Different pulse schemes can result in radically different . Some researches use

4.3   Quantum sensing setup

Executing all of the aforementioned protocols requires a sensing setup with some specific capabilities. This section discusses the devices that make up the setup and the functionalities require by each protocol.

A high-level diagram of the quantum sensing system can be seen in Figure 4.5. There are 2 input devices in the system, but most protocols exclusively use the function generator. On the other hand, only a single lock-in amplifier is used as an output device for all measurements.

The blue boxes show the components responsible for sending and receiving light signals. They constitute the core of the setup. Waveforms are generated by the function generator, no matter the protocol. Using a current driver, the laser is then used to illuminate the diamond sample. The resulting luminescence is then measured by the photodetector and processed by the lock-in amplifier. All protocols need this part of the setup, however they utilize it differently.

Microwave generation, when needed, starts with a TTL signal from the function generator or a frequency sweep using a dedicated device. Out of all protocols, only CW-ODMR requires a sweep. The antenna then broadcasts the signal, while the switch isolates the signal generator from it.
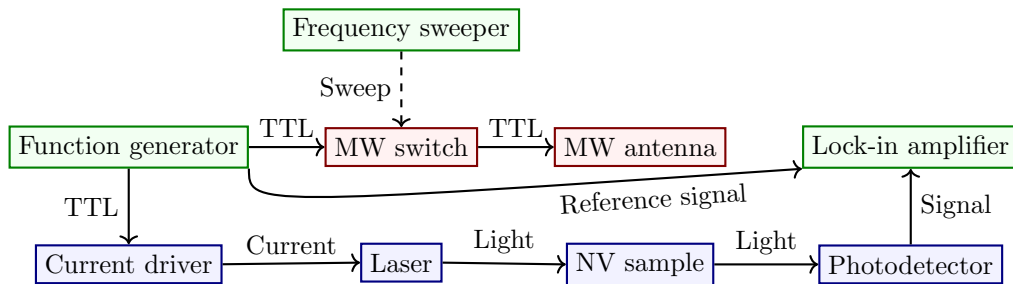

Figure 4.5: High-level overview of the quantum sensing setup

4.4   Lock-in amplification

As a means of retrieving data, lock-in amplification is the most suitable for the setup due to its relatively low cost, signal retrieval capabilities and the possibility of using one amplifier for several setups.
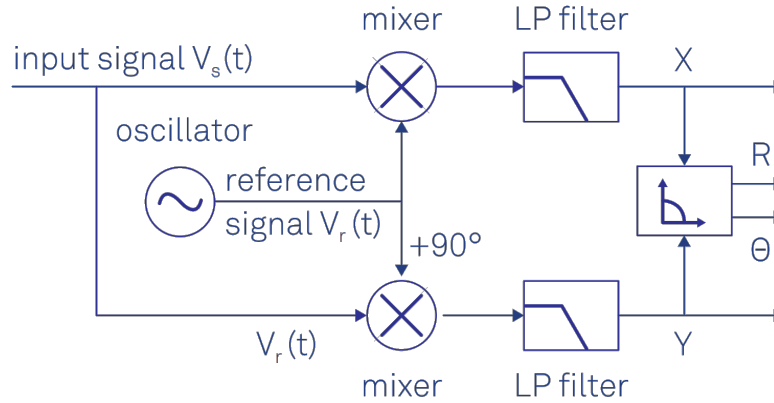

Figure 4.6: High-level diagram of a lock-in amplifier (image credit to Zurich Instruments [11])

Figure 4.6 shows an overview of how lock-in amplification works. Simply put, the amplifier receives a signal V_s and extracts the data at the frequency of a reference signal V_r. To explain this more thoroughly, lock-in amplification utilizes the fact that every signal is made of periodic waves, which are equal to zero when averaged.

$$V_s = R \cos\left(\omega_s t + \theta\right) = \frac{R}{2}e^{i(\omega_s t + \theta)} + \frac{R}{2}e^{-i(\omega_s t + \theta)} \tag{4.2}$$

Equation 4.2 shows how the mathematical expression of a sine wave signal, where ω_s is the frequency and θ is the phase of the signal. Using the trigonometric identity $\cos x = \frac{1}{2}(e^{ix} + e^{-ix})$, the signal can be represented in terms of complex numbers.

$$V_r = e^{-i\omega_r t} \tag{4.3}$$

In Equation 4.3, a simplified reference signal is shown. Real applications might require more complex reference signals, but V_r is perfect for demonstrating the lock-in principle.

$$V_m = V_s V_r = \frac{R}{2}e^{i(\omega_s - \omega_r)t + \theta} + \frac{R}{2}e^{-i(\omega_s + \omega_r)t + \theta} \tag{4.4}$$

Finally, Equation 4.4 shows the product of the signal V_s and the reference V_r. In the case of $\omega_s = \omega_r$, there is a signal at 0 Hz and another one at $2\omega_s$ Hz. The latter, however, should be attenuated to an undetectable level by the low-pass filters shown in Figure 4.6. This way, both the unwanted signal appearing at double the frequency and all of the noise at different frequencies is attenuated.

4.5   Photodetection

Photodetection is how the NV photoluminescence is measured, effectively turning light into current using a photodiode. However, a bare photodiode cannot be connected to a lock-in amplifier, because it functions as a current generator. This is where the photodetection PCB comes in. Its purpose is to transform the current into voltage and then amplify the resulting signal to the necessary voltage level.

4.6   Photodiodes

At the heart of the photodetector lies the photodiode. It is what turns light into current and drives the TIA that follows it. While the specifications of the diode are not the most important part of the photodetector circuit, they still need to be discussed, due to the impact the two ways of biasing can have on the circuit.

An exceedingly common photodiode configuration,

4.6.1 TIA design

Designing the photodetector is mostly about creating a TIA, which is a tool used for converting current to voltage, and specifically tuning its parameters so that it works with the selected photodiode under operating conditions.
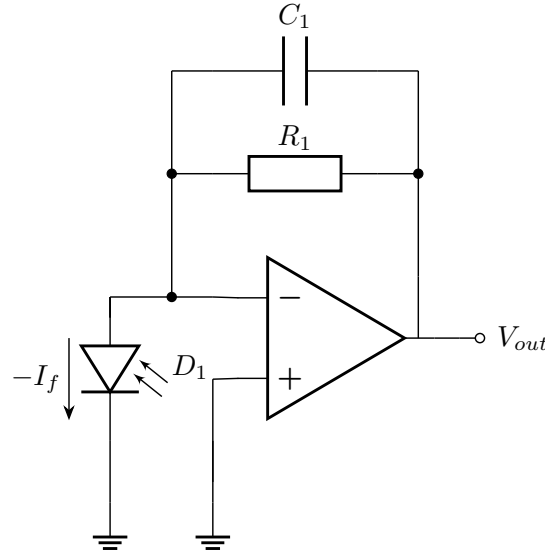

Figure 4.7: Basic TIA circuit

The basic circuit, shown in Figure 4.7, is all that is required for photodetection. Following the guidelines for making a TIA set by Texas Instruments [12], all the parameters of the circuit can be calculated.

$$R_1 = \frac{V_{o\ max}}{I_{o\ max}} \text{ assuming } V_{o\ min} = 0\text{V} \tag{4.5}$$

The resistor R_1 determines the transimpedance gain of the amplifier. Equation 4.5 shows how its value can be calculated by using the output voltage and input current. It should be noted that the minimum output voltage is always 0 in this use case.

$$C_1 = \frac{1}{2\pi R_1 f_{rc}} \tag{4.6}$$

The capacitance of C_1 can be calculated using the resistance of R_1 and the cutoff frequency f_{rc}, as shown in Equation 4.6.

In addition, a non-inverting amplifier can be added, to increase the gain of the circuit even more, without affecting the phase. Figure 4.8 shows how it can be connected to the output of the TIA from Figure 4.7.

Equation 4.7 is used to calculate the gain of second amplification stage. The formula is derived from the voltage divider formed by the two resistors and the fact that $V_{ot} = V_-$.

$$A_{nia} = \frac{Vout}{Vot} = 1 + \frac{R_3}{R_2} \tag{4.7}$$

The design is based on circuits provided by the client. At their request, the first version of the PCB is an exact replica of the original circuit.
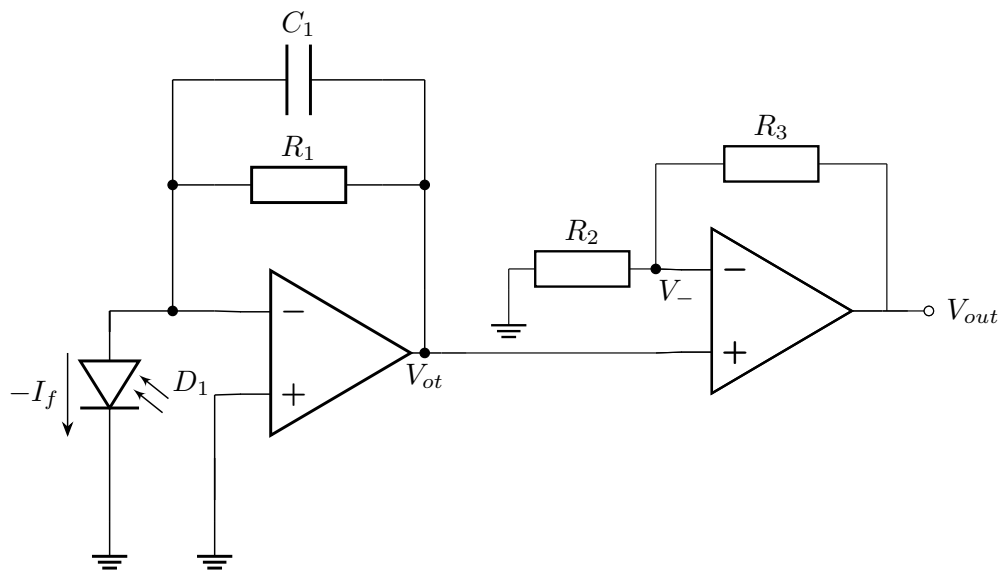
Figure 4.8: TIA with non-inverting output amplification

Chapter 5

Technical design

5.1   Quantum sensing setup

5.2   Photodetector design

As an integral part of the sensing setup, the photodetector needs a lot of attention. Good amplification is crucial to increasing the SNR of the quantum setup. Based on the design ideas presented in the functional design (see Chapter 4.6.1), the photodetection circuit can be drawn up.

5.2.1   First iteration

As previously mentioned, the first iteration of the PCB uses component values provided by the client. There is no specific information for the design process, aside from the fact that the original designer made the photodetector for input currents in the range of several nanoamperes. Such low inputs require high R_1 values, however increasing the resistor value results in more biasing current going to the amplifier and a more limited dynamic range [13]. Furthermore, it is entirely possible that the original design did not thoroughly consider the bandwidth needed for different protocols, as CW-ODMR setups do not require broad bandwidths [14]. Biasing is another concern with this photodiode setup. The configuration shown in Figures 4.7 and 5.1 has the diode in the photovoltaic mode, which is suitable for low-frequency, low-light operation. In spite of this setup being suited to CW-ODMR, pulsed protocols require micro to nanosecond precision

5.2.2   Second iteration

Due to time constraints, this iteration uses the same topology as the first one. That being said, it is still designed analytically, taking into account the general practices, but also considering more subtle factors that might hinder the performance of the system. This section uses the mathematical principles presented in [15–17] to optimize the design of the existing amplifier.

Introducing the real-world parasitic capacitances to the ideal TIA shown in Figure 4.7 results in the circuit in Figure 5.1. The diode capacitance C_d, combined with the differential and common-mode capacitances of the amplifier (C_{df} and C_{cm}), contributes a significant amount of capacitance to the circuit and can result in instability [18].

$$C_i = C_d + C_{df} + C_{cm} \tag{5.1}$$

The combined input capacitance (Equation 5.1) is needed when solving the equation arising from Kirchhoff's Current Law (KCL) at the inverting input of the amplifier. Z_1 (Equation 5.2), or the combined impedance of R_1 and C_1, is another prerequisite for deriving the transimpedance Z_t using KCL. Additionally, the open-loop gain A_{ol} is needed for the derivation of the transimpedance. Equation 5.3 shows the open-loop gain, expressed with the Direct Current (DC) open-loop gain A_o and the open-loop cutoff frequency ω_o, which is equivalent to $\frac{v_{out}}{v_{in}}$.

$$Z_1(s) = \frac{1}{\frac{1}{R_1} + sC_1} \tag{5.2}$$

$$A_{ol}(s) = A_o \frac{\omega_0}{s + \omega_0} = \frac{v_{out}}{v_{in}} \tag{5.3}$$
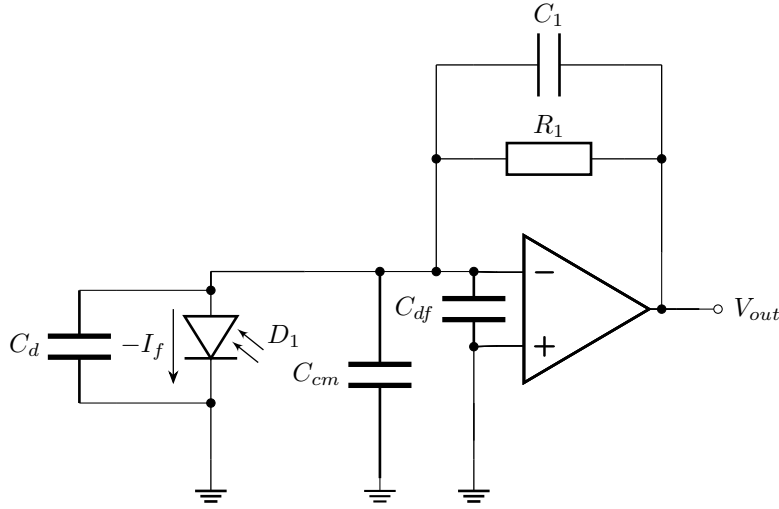
Figure 5.1: Parasitic capacitances in a TIA circuit

Finally, the values in the KCL equation (Equation 5.4) can be substituted, from which Z_t can be derived, as seen in Equation 5.5.

$$i_f = \frac{v_i}{\frac{1}{sC_i}} + \frac{v_{in} - v_{out}}{Z_1(s)} \tag{5.4}$$

$$Z_t(s) = \frac{v_{out}}{i_f} = (R_1 \frac{A_o}{1+A_o}) \frac{\frac{\omega_o(1+A_o)}{(C_i+C_1)R_1}}{s^2 + s\frac{1+\omega_o(C_i+(1+A_o)C_1)R_1}{(C_i+C_1)R_1} + \frac{\omega_o(1+A_o)}{(C_i+C_1)R_1}} \tag{5.5}$$

Before moving on to the pole analysis, the impact of the quality factor Q on the system response should be considered (see Equation 5.12). Two system poles present when $Q > 0, 5$. For $Q = \frac{\sqrt{3}}{3}$, the system has a Bessel response, which has the flattest group delay, however, if $Q = \frac{\sqrt{2}}{2}$, then the system has a Butterworth response, which means it has the flattest possible amplitude response. Although the group delay is not as important as the amplitude response, a Bessel response also results in smaller amount of overshoot and less jitter, which is why it is preferred.

$$H(s) = H_0 \frac{(-s_1)(-s_2)}{(s-s_1)(s-s_2)} = H_0 \frac{s_1 s_2}{s^2 + s(-s_1 - s_2) + s_1 s_2} \tag{5.6}$$

Based on this consideration, the poles can be found using the general form of a second order transfer function, shown in Equation 5.6. The general form also makes it obvious that the DC gain $H_0 \approx R_1$, assuming that A_0 is very big.

$$\begin{cases} -s_1 - s_2 = \frac{1+\omega_o(C_i+(1+A_o)C_1)R_1}{(C_i+C_1)R_1} \\ s_1 s_2 = \frac{\omega_o(1+A_o)}{(C_i+C_1)R_1} \end{cases} \tag{5.7}$$

Taking the general-equation poles and their counterparts from the Z_t expression yields the system of equations shown in Equation 5.7. Solving for one pole first results in a quadratic equation with roots shown in Equation 5.8.

$$s_{1,2} = -\frac{1+\omega_o(C_i(1+A_o)C_1)R_1}{2(C_i+C_1)R_1} \left(1 \pm j \sqrt{\frac{4\omega_o(1+A_o)(C_i+C_1)R_1}{(1+\omega_o(C_i+(1+A_o)C_1)R_1)^2} - 1} \right) \tag{5.8}$$

$$s_{1,2} = -\frac{3}{2}(1 \pm j\frac{\sqrt{3}}{3}) \tag{5.9}$$

Achieving a critically-damped system, can be done by getting the roots of the general form of a Bessel filter (as seen in Equation 5.9) and using the imaginary parts to get Equation 5.10. This expression can be solved with the quadratic formula again, finally resulting in an answer for the compensating capacitor.

$$\frac{4\omega_o(1+A_o)(C_i+C_1)R_1}{(1+\omega_o(C_i+(1+A_o)C_1)R_1)^2} = \frac{4}{3} \tag{5.10}$$

$$C_1 = \frac{-2\omega_o R_1 C_i \pm \sqrt{12 A_o C_i R_1 \omega_o - 3}}{2\omega_o R_1 (1 + A_o)} \tag{5.11}$$

Although Equation 5.11 says there are two solutions for the capacitor, the term under the square root will always be much bigger than the rest of the numerator[1], effectively determining the sign of the roots. Simply put, this leaves only one root possible, as capacitors cannot have negative capacitance values.

To further characterize the system, the cutoff frequency ω_c and damping factor Q can be calculated, because the system adheres to the general form, shown in Equation 5.12. Substituting in the pole expressions from Equations 5.6 and 5.7.

$$H(s) = H_o \frac{\omega_c^2}{s^2 + s\frac{\omega_c}{Q} + \omega_c^2} \tag{5.12}$$

$$\begin{cases} \omega_c = \sqrt{\frac{\omega_o(1+A_o)}{(C_i+C_1)R_1}} \\ Q = \omega_c \frac{(C_i+C_1)R_1}{1+\omega_o(C_i+(1+A_o)C_1)R_1} \end{cases} \tag{5.13}$$

In the process of designing the TIA circuit, the noise should be considered. Figure 5.2 shows the thermal noise generated by the resistor (modeled as the current source i_{nR}) and the differential noise of the amplifier (modeled as the current source i_{nA})[2].
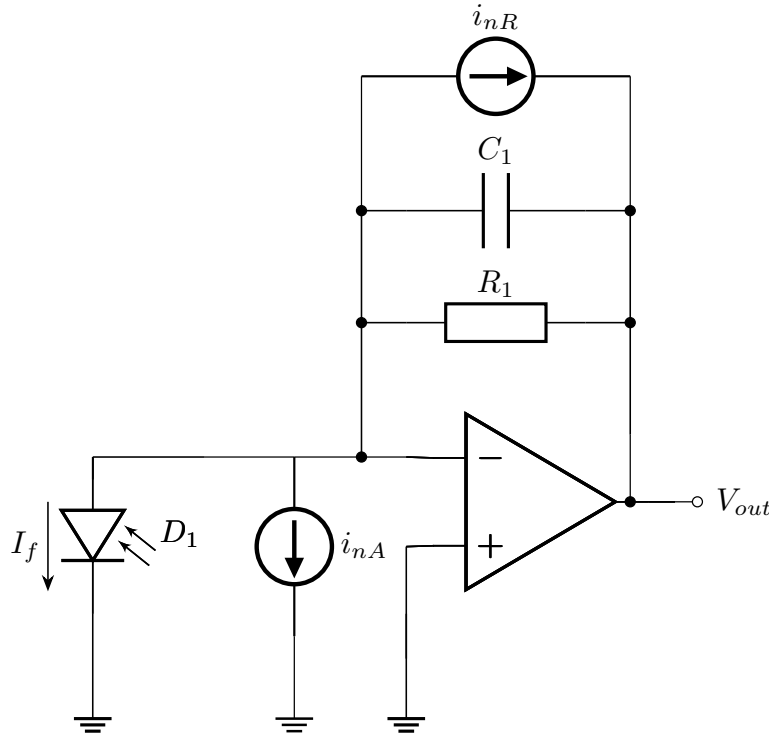

Figure 5.2: Noise sources in a TIA circuit

Calculating i_{nR} can be done using the Johnson-Nyquist formula, as shown in Equation 5.14. Given the fact that the temperature T and noise cutoff frequency δf cannot be modified in this case, R_1 is the only variable that can be used to lower the thermal noise current.

$$i_{nR} = \sqrt{\frac{4kT\Delta f}{R_1}} \tag{5.14}$$

Combining the noise sources leads to Equation 5.15, which also shows that the noise can be modeled as voltage sources.

$$i_n(f) = \sqrt{i_{nR}^2 + i_{nA}^2} \Leftrightarrow v_n(f) = \sqrt{v_{nR}^2 + v_{nA}^2} \tag{5.15}$$

---

[1]Assuming real-world amplifier and diode specifications, and realistic transimpedance gain requirements

[2]Other noise generators, like the gate shot noise, channel noise and induced gate noise can also be calculated, but because they largely depend on the underlying technology of the Field-Effect Transistor (FET) op amp, they have not been investigated

In order to get a better understanding of the noise, its transfer function can be calculated in much the same way as the transimpedance (Equations 5.3 - 5.5), leading to Equation 5.16. While it might not be immediately obvious from the mathematical expression, the noise gain is 0 dB at low frequencies, but it peaks when $f \approx f_c$. Chapter 5.3.2 shows the noise frequency response obtained from the system equation.

$$H_n(s) = \frac{v_o}{v_n} = \frac{A_o \omega_o (s + \frac{1}{(C_i + C_1)R_1})}{s^2 + s(\frac{1}{(C_i + C_1)R_1} + \omega_o(1 + A_o \frac{C_1}{C_i + C_1})) + \frac{\omega_o(1 + A_o)}{(C_i + C_1)R_1}} \tag{5.16}$$

5.2.3   Third iteration

While the second version of the photodetector focuses on improving the TIA performance, the third iteration is more about adapting the design for the setup. The most important considerations for the setup are function and size. Form factor constraints arise from the fact that the setup needs to be as small and adhere to the Thorlabs mounting standard. Photodetection also needs to not require many external connections or ideally be standalone. This is feasible for the data flow, as the photodetection PCB only needs light and an output to work. Unlike the data connections, version two of the design has a suboptimal power delivery system, as it uses three pins for the supply of power.

Three alternatives methods for power delivery were considered, all of which only need power and ground to work. The first one is an onboard split-rail power supply, which would take the power input and would output a fixed positive and negative voltage. Figure 5.3 shows an example of what a split-rail supply implementation might look like. There are also external option [19], which might be necessary in the future, if the setup size needs to be reduced even more.
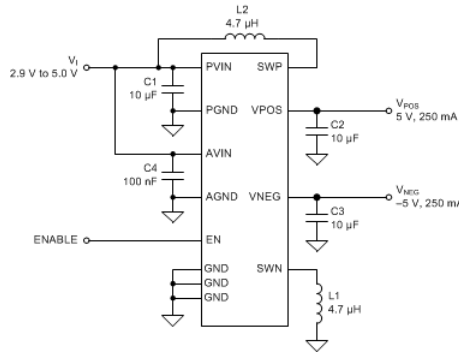

Figure 5.3: Example of a split-rail power supply implementation using the TPS65133 IC (image credit to [20])

A simpler solution would be to use a virtual ground driver Integrated Circuit (IC), as it would provide a reference point at half of the supply voltage. Such a supply would also be good for decreasing the size, as the PCB needs minimal additions to satisfy the power needs of the photodetector. Additionally, a virtual ground circuit, which behaves similarly, can be made using two voltage regulators. The example in Figure 5.4 is a slightly more stable implementation
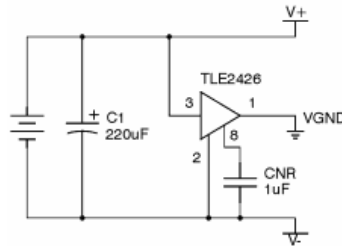

Figure 5.4: Example of a virtual ground driver using the TLE2426 IC (image credit to [21])

Another possibility is to implement a charge pump, which inverts the input voltage. This setup would only need half of the input voltage required for the virtual ground solution, effectively enabling it to be powered via a standard Universal Serial Bus (USB) connector.
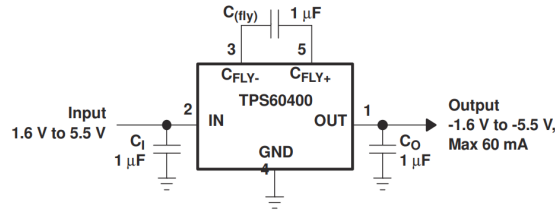
Figure 5.5: Example of a charge pump inverter using a TPS6040x family IC (image credit to [22]

	Split-rail power supply	Virtual ground	Charge pump
IC	TPS65133	TLE2426	TPS60400
V_{in} (V)	5	10	5
V_{out} (V)	±5	±5	-5
I_{out} (mA)	250	40	60
Current draw (μA)	15	300	210

Table 5.1: Comparison of power supply options

The specifications of the different power supply solutions are shown in Table 5.1, from which can be deduced that there is a correlation between complexity and performance. The split-rail power supply, as the most complex solution, has the biggest current output range and lowest current consumption, but as illustrated in Figure 5.3, there are a number of other components that are required for proper implementation. In contrast, the virtual ground supply concept has relatively poor specifications compared to the other options, but it is the only solution that does not employ a switching mechanism, thus avoiding any possible noise. Lastly, the charge pump inverter offers reasonable performance, while not needing as many extra components as the split-rail supply. Furthermore, the

5.3   Photodetection simulation

Simulation is an important part of the designing process, as digital models of devices can be more detailed than the mathematical models presented thus far. Using different simulation programs, the real-world performance can be approximated and the math can be validated.
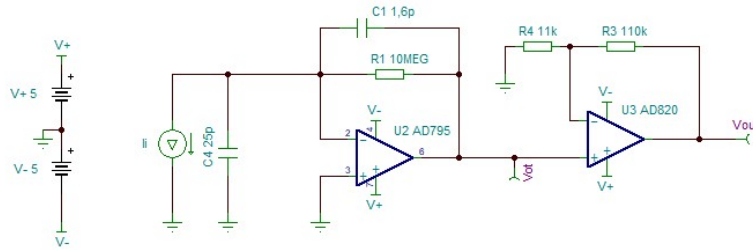
5.3.1   First iteration

Figure 5.6: First iteration of the photodetector circuit

Figure 5.6 shows the schematic of the circuit. The capacitor C_4, as well as the current source I_1 are used to simulate the behavior of a photodiode.

Tina-TI was used to simulate and visualize the DC gain and frequency response of the system, as seen in Figure 5.7. The signals V_{ot} and V_{out} correspond to the output of the transimpedance and non-inverting amplification stage respectively. The AC plot (Figure 5.7a) shows the cutoff, at 10,77 kHz, and the gain inside the gain bandwidth, which is 160,82 dB. The DC plot (Figure 5.7b) shows the voltage with respect to the current and demonstrates the linearity of the system in the range of 0 to 46,31 nA. After V_{out} reaches 5 V, the output remains fixed, because it cannot exceed the voltage provided to the amplifier.
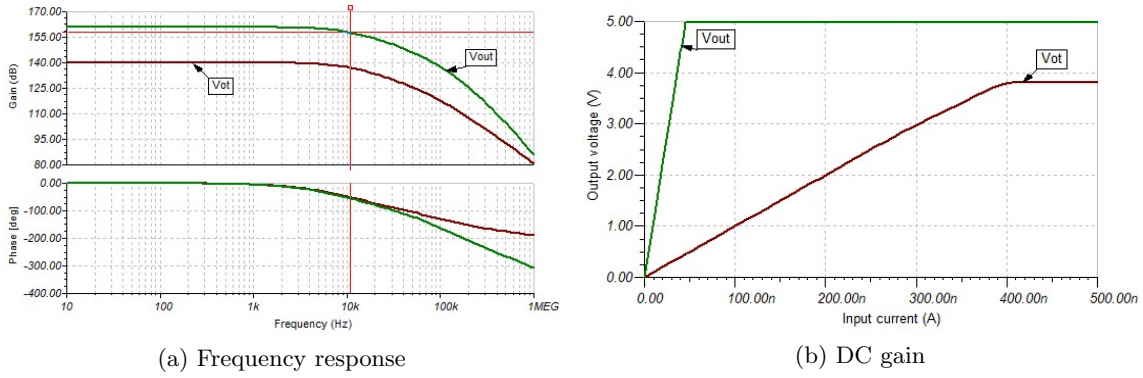
(a) Frequency response

(b) DC gain

Figure 5.7: Simulation of the first iteration of the photodetector

5.3.2 Second iteration

A MATLAB script was written to calculate the component values based on the calculations in Chapter 5.2.2.

MATLAB calculates the component values with high precision and sourcing components with the exact values is not feasible, which is why components with standard values will be used in the setup. Simulations with standardized components were also done to compare the mathematically-ideal setup to the one in practice.

TIA version	v2 (Ideal)	v2 (Real.)	v1
C_1 (pF)	0,969 04	1	1,6
f_c (kHz)	22,0768	21,167	11,2422
Q	0,577 35	0,559 96	0,354 87

Table 5.2: Photodetector parameters with a 10 MΩ feedback resistor R_1

Table 5.2 contains the MATLAB calculation results and shows the values of f_c and Q when only C_1 changes. R_1 is kept the same, as it is equivalent the DC transimpedance Z_{tDC}[3]. Importantly, the results show that the previous iteration had an overdamped response. Although the quality factor with realistic component values is also lower than the ideal $Q = \frac{\sqrt{3}}{3}$, the system sill behaves approximately like a Bessel filter.

Using these values, the system model was calculated and plotted in Figure 5.8. Certain differences can be seen between the two iterations. Most notably, the cutoff frequency f_c of the first iteration is somewhat smaller than that of the second iteration. Furthermore, it can be observed that both the ideal and realistic versions of the system behave similarly.

5.4 Photodetection implementation

Creating the physical PCB is a more straightforward process than the design and simulation, but it still needs to be discussed.

5.4.1 First iteration

Figure 5.9 shows the back side of the PCB. It hosts all components, except for the photodiode, which sits unobstructed on the front side. Requirements for the physical dimensions were also set by the client. The PCB needs to fit the Thorlabs mount standard, since the rest of the setup also uses it.

5.4.2 Second iteration

Due to the fact that the topology of the first iteration was kept, the PCB does not need any modifications in order to work with the circuit parameters. However, after a discussion with the client, a ground plane was added. Usually such an addition would be needed in high-speed and/or high-power use cases, but the circuit only deals with low-speed, very-low-power signals. The reason

---

[3]For realistic op-amps, $\frac{A_o}{A_o+1} \to 1$, which means $Z_{tDC} \equiv R_1$ can be assumed to simplify explanations
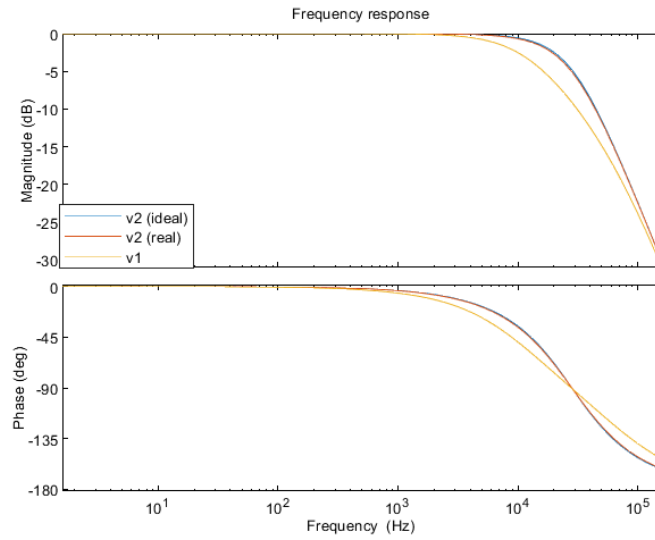
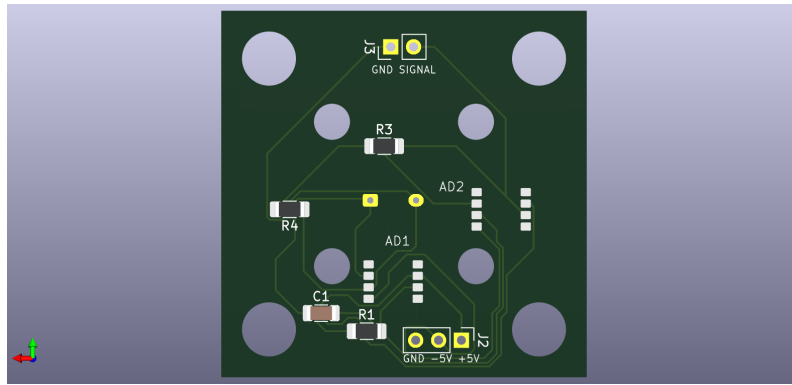Figure 5.8: Bode plot of the system with different capacitors

Figure 5.9: First iteration of the photodetection PCB

for the ground plane in the updated design is broader quantum protocol support. While CW-ODMR operates at low frequencies, future expansion of the sensing setup might require support for different high-speed pulsing sequences. In that case, the component values can be modified again, without the need for making a new board. Figure 5.10 shows the new board design. The updated board also has better routing than the previous version, which was done to optimize the noise performance.
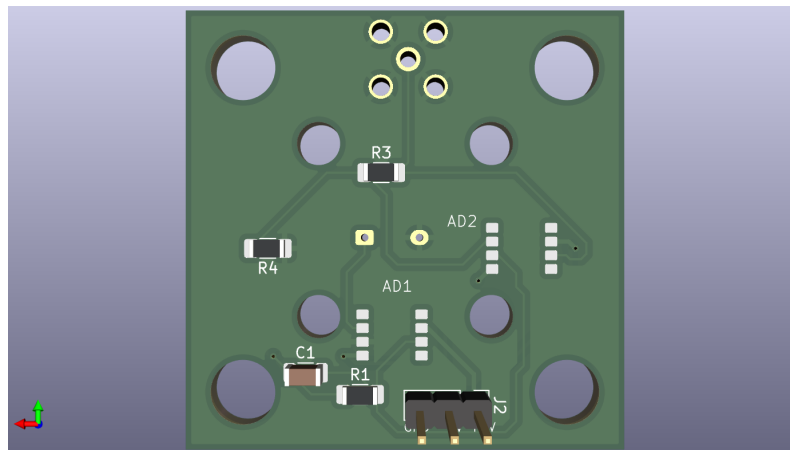
Figure 5.10: Second iteration of the photodetection PCB

Chapter 6

Testing results

Number	Task	Status
1.1	Deploy and configure at least one OpenRemote instance	Completed
1.2	Establish communication to the OpenRemote instance using the HTTP and MQTT protocols	Completed
2.1	Simulate IoT devices (smart homes) that send and receive concurrent MQTT data to OpenRemote and measure the latency of the transmissions	Completed
2.2	Create a physical IoT device setup using a platform like ESP32 or Arduino and recreate the tests from Goal 1.2	Completed
2.3	Integrate and test OpenRemote's Prophet project	Not started
2.4	Test performance and create visualizations	Completed
3.1	Document technical progress	Completed
3.2	Reflect on personal and professional development	Completed
3.3	Communicate project results	Ongoing

Table 6.1: Goal completion

6.1   Test goals and performance metrics

Metric	API	Unit(s) of measurement	Explanation
Device provisioning latency	HTTP	seconds (s)	Time between creation request and confirmation
Message loss percentage	MQTT	percent (%)	Percent of MQTT messages which are lost
Resource usage	-	percent (CPU %, RAM %)	CPU and RAM usage when running tests

Table 6.2: Metrics of the OpenRemote scalability tests

6.2   Test setup

6.3   Results and discussion

6.4   Known limitations

Chapter 7

Conclusion

Chapter 8

Recommendations

Appendix A

Code

Glossary

DC Direct Current 16, 17, 21

ECAD Electronic Computer-Aided Design 6

FET Field-Effect Transistor 18

GUI Graphical User Interface 6

IC Integrated Circuit 19

KCL Kirchhoff's Current Law 16, 17

MRI Magnetic Resonance Imaging 10
MW Microwave 5, 6

NV Nitrogen Vacancy 5, 6, 8–11, 13

ODMR Optically Detected Magnetic Resonance 5, 29
   CW-ODMR Constant-Wave ODMR 5, 6, 10–12, 16, 22
   P-ODMR Pulsed ODMR 5, 10, 12
OLIA Open Lock-In Amplifier 5–7

PCB Printed Circuit Board 7, 13, 19, 21

SNR Signal-to-Noise Ratio 7, 16

TIA Transimpedance Amplifier 5, 13–18
TTL Transistor-Transistor Logic 5, 12

USB Universal Serial Bus 19

Bibliography

[1]   Wikipedia contributors, *Nitrogen-vacancy center — Wikipedia, the free encyclopedia*, [Online; accessed 3-September-2025], 2025. [Online]. Available: https://en.wikipedia.org/w/index.php?title=Nitrogen-vacancy_center&oldid=1301369588.

[2]   Wikipedia contributors, *Photoluminescence — Wikipedia, the free encyclopedia*, https://en.wikipedia.org/w/index.php?title=Photoluminescence&oldid=1309081879, [Online; accessed 4-September-2025], 2025.

[3]   Wikipedia contributors, *Optically detected magnetic resonance — Wikipedia, the free encyclopedia*, https://en.wikipedia.org/w/index.php?title=Optically_detected_magnetic_resonance&oldid=1301371272, [Online; accessed 6-October-2025], 2025.

[4]   V. K. Sewani et al., "Coherent control of nv- centers in diamond in a quantum teaching lab," *American Journal of Physics*, vol. 88, no. 12, pp. 1156–1169, 2020.

[5]   A. Haque and S. Sumaiya, "An overview on the formation and processing of nitrogen-vacancy photonic centers in diamond by ion implantation," *Journal of Manufacturing and Materials Processing*, vol. 1, no. 1, p. 6, 2017.

[6]   A. J. Harvie and J. C. de Mello, "Olia: An open-source digital lock-in amplifier," *Frontiers in Sensors*, vol. 4, p. 1 102 176, 2023.

[7]   Z. Song et al., "Enhancing fluorescence of diamond nv- centers for quantum sensing: A multi-layer optical antireflection coating," *Diamond and Related Materials*, vol. 141, p. 110 584, 2024.

[8]   S. Saijo et al., "Ac magnetic field sensing using continuous-wave optically detected magnetic resonance of nitrogen-vacancy centers in diamond," *Applied Physics Letters*, vol. 113, no. 8, 2018.

[9]   Y. Zhang et al., "High-sensitivity dc magnetic field detection with ensemble nv centers by pulsed quantum filtering technology," *Optics Express*, vol. 28, no. 11, pp. 16 191–16 201, 2020.

[10] J. Jones, W. Howden, A. Murphy, et al., *T1 relaxation time*. [Online]. Available: https://doi.org/10.53347/rID-25821.

[11] Z. Instruments, "Principles of lock-in detection and the state of the art. 2016," *Internetadresse: https://www. zhinst. com/sites/default/files/li_primer/zi_whitepaper_principles_of_lock-in_detection. pdf. Zuletzt aufgerufen am*, vol. 17, 2018.

[12] P. Semig, *Transimpedence amplifier circuit*. [Online]. Available: https://www.ti.com/lit/an/sboa268b/sboa268b.pdf.

[13] B. Black and G. Brisebois, *Transimpedance amplifiers for wide range photodiodes have challenging requirements*, 2021.

[14] B. Acharya, "Compact integration of nv-based diamond quantum sensors using a small-size photodiode and on-board transimpedance amplifier," Ph.D. dissertation, Wichita State University, 2025.

[15] E. Margan, "Transimpedance amplifier analysis," *no*, vol. 1, pp. 1–19, 2012.

[16] E. Säckinger, *Analysis and design of transimpedance amplifiers for optical receivers*. John Wiley & Sons, 2017.

[17] L. Horsthemke et al., "All optical magnetometry with nitrogen vacancy centers in diamonds," Ph.D. dissertation, Universidad de Granada, 2025.

[18] S. Cherian, "What you need to know about transimpedance amplifiers–part 1," *Texas Instruments Incorporated*, 2016.

[19] L. Clark, *Adafruit tps65131 split power supply boost converter*, 2025. [Online]. Available: https://cdn-learn.adafruit.com/downloads/pdf/adafruit-tps65131-split-power-supply-boost-converter.pdf.

[20] *Tps65133 ±5-v, 250-ma dual-output power supply*, SLVSC01A, Rev. A, Texas Instruments, Jun. 2013.

[21] TangentSoft. "Virtual ground circuits. "[Online]. Available: https://tangentsoft.com/elec/vgrounds.html.

[22] T. Instruments, *Tps6040x unregulated 60-ma charge pump voltage inverter*, 2015.